Supplymental Material

Achieving High Strength and Ductility in Refractory Multi-Principal-Element Alloys via Electronic Structure Tuning

Hailong Huang[1], Prashant Singh[1], Duane D. Johnson[1,2], Dishant Beniwal[3,+], Pratik K. Ray[3], Gaoyuan Ouyang[1], Luke Gaydos[1,2], Trevor Riedemann[1], Tirthesh Ingale[4], Vishal Soni[4], Rajarshi Banerjee[4], Thomas Scharf[4], Ping Lu[5], Frank W. DelRio[5], Andrew Kustas[5], John Sharon[6], Ryan Deacon[6], Syed I.A. Jalali[7], Michael Patullo[7], Sharon Park[8], Kevin Hemker[7,8], Ryan T. Ott[1], and Nicolas Argibay[1,2,*]

[1] *Division of Materials Science and Engineering, Ames National Laboratory, IA, USA*
[2] *Department of Materials Science and Engineering, Iowa State University, IA, USA*
[3] *Metallurgical and Materials Engineering, Indian Institute of Technology Ropar, Rupnagar, PB, India*
[4] *Department of Materials Science and Engineering, University of North Texas, Denton, TX, USA*
[5] *Material, Physical, and Chemical Science Center, Sandia National Laboratories, Albuquerque, NM , USA*
[6] *RTX Technology Research Center, East Hartford, CT, USA*
[7] *Department of Mechanical Engineering, Johns Hopkins University, Baltimore, MD, USA*
[8] *Department of Materials Science & Engineering, Johns Hopkins University, Baltimore, MD , USA*
+ Current address: *X-ray Science Division, Argonne National Laboratory, Lemont, IL, USA*

Corresponding author: nargibay@ameslab.gov

Cluster Analysis for atom probe tomography data

The APT data was analyzed first by visually examining the raw ion maps to observe any obvious segregation. An in-depth cluster analysis using frequency distribution and radial distribution analyses is carried out to investigate any clustering at a finer scale if no obvious segregation was observed in the ion map. A smaller volume of 30 nm by 40 nm was cropped from the center of the original reconstruction for cluster analysis to avoid interference caused by any hydrogen or gallium contamination near the tip surface. For frequency distribution analysis, the volume is divided into voxels each containing N number of ions (N=100 in this case). The frequency distribution is basically a histogram with mole fraction of each element in a voxel plotted as a function of concentration. Comparison between the measured distribution of the elements with theoretical distribution can indicate the presence of any clustering for each element. Radical distribution function (RDF) calculates the concentration of elements as a function of radial distance from a specified center element (Ti, in this case). When the frequency distribution or radial distribution analysis indicates the possibility of clustering, cluster analysis using a maximum separation method is performed to reveal the qualitative and quantitative details of the clusters. The maximum separation distance between the clustered element(s) (d_{max}) and a minimum number of ions (N_{min}) in the cluster is determined based on the nearest neighboring distribution, cluster size and count distributions[1,2]. The cluster analysis was performed on the furnace-cooled and oil quenched sample with similar level of impurities to identify any difference in clustering tendencies. Both RDF plots indicate positive interaction between Ti-Ti and T-V pairs, and negative interaction between Ti-Nb and Ti-Ta pairs below approximately 1.0 nm, suggesting the same clustering tendency in both cases. A much profound Ti-Ti clustering is observed in furnace-cooled specimen, revealing an increase in chemical ordering after slow cooling in $Nb_4Ta_4V_3Ti_1$ alloy. The Ti rich clustered-ordering domains in furnace cooled sample with a d_{max} of 0.45 nm and a N_{min} of 12 are deduced through cluster analysis.

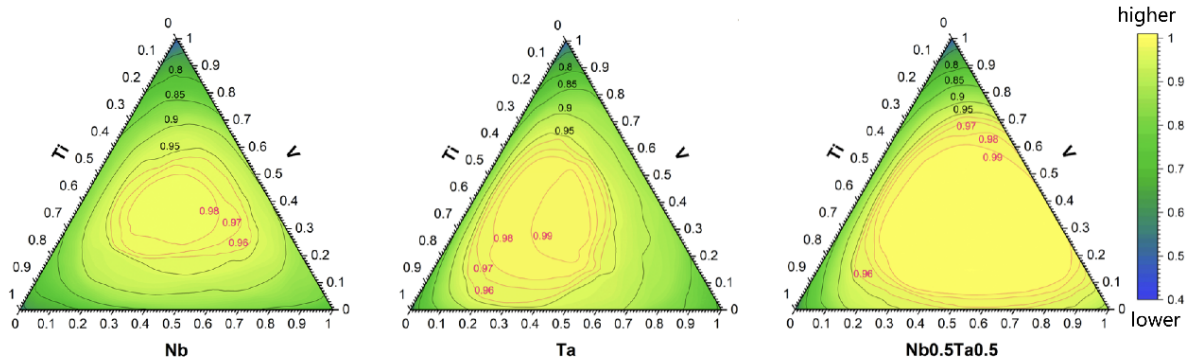

Figure S1. **Complementary ternary and pseudo-ternary phase diagrams show BCC phase stability evolution with changing composition**. The equimolar Nb-Ta ratio is shown to produce the largest region of high single-phase BCC stability.

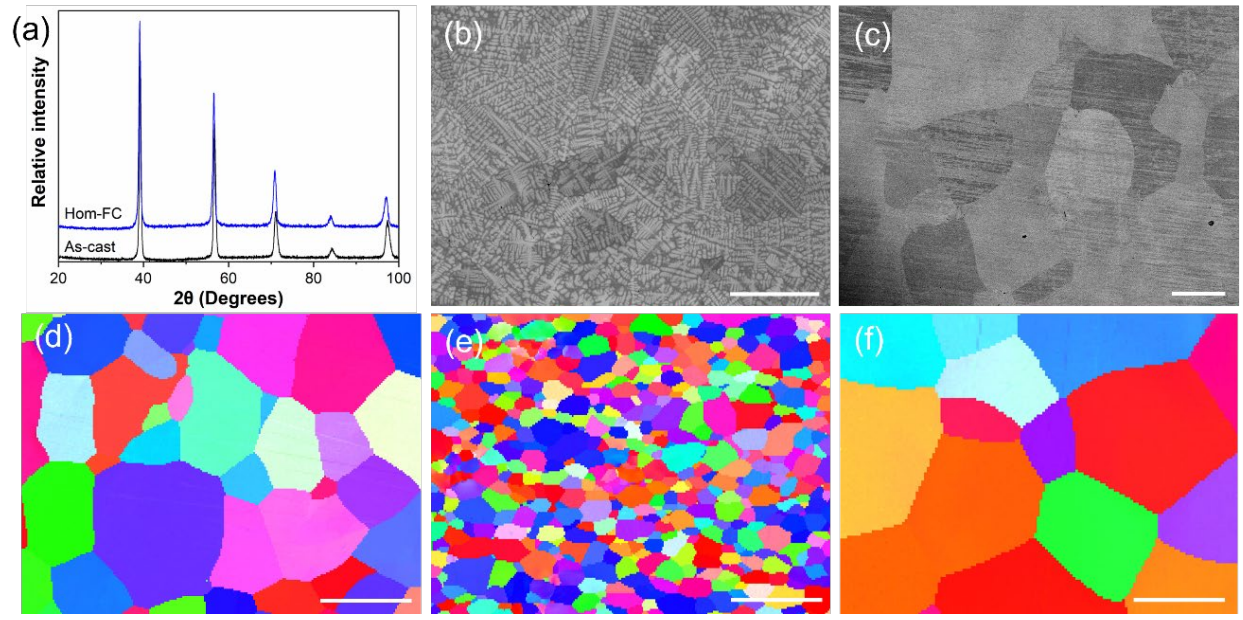

Fig. S2. Microstructure characterization of $Nb_4Ta_4V_3Ti_1$ under different thermal processing. a, the X-ray diffraction patterns of the as-cast and 1400 °C@24h homogenized and furnace cooled sample demonstrate the single-phase BCC structure with lattice parameters of 3.2937 Å and 3.3026 Å, respectively. **b,** SEM image of the as-cast shows typical dendritic segregation. **c,** SEM image of the homogenized specimen showing coarse grains. **d-e**, EBSD inverse pole figures (IPF) for the alloy at the homogenized, 1200 °C@24 recrystallized and quenched, and oxygen-reducing annealed and quenched states respectively, indicating near-equiaxed grain morphologies with various grain size. For simplicity, the scale bars are 100 μm.

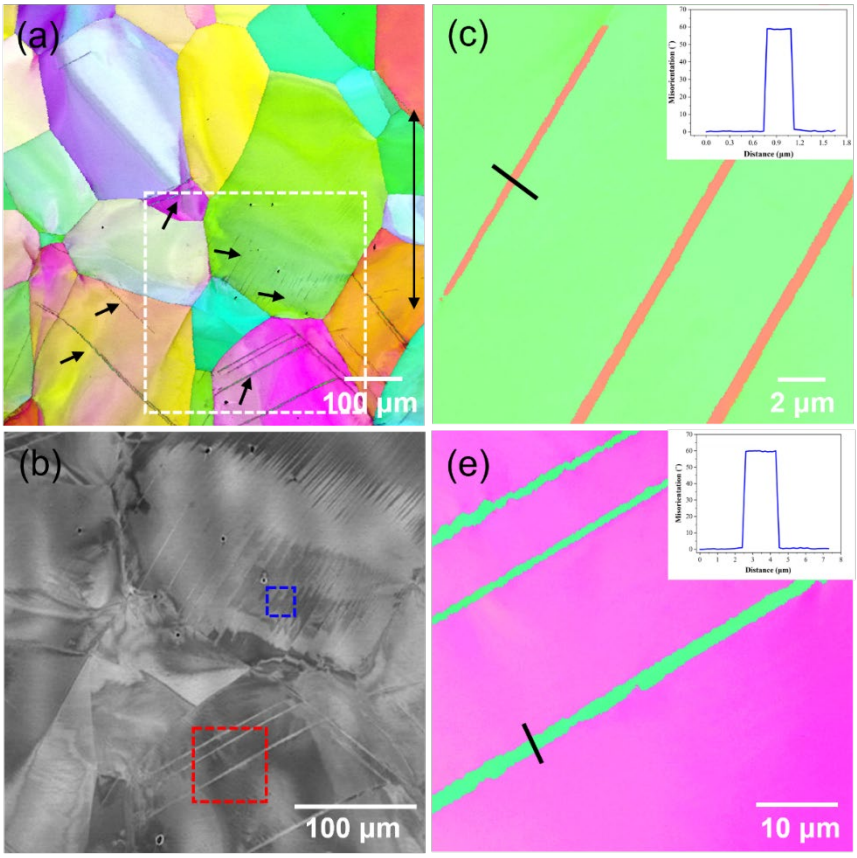

Fig. S3. EBSD and ECCI images of the gauge section of homogenized sample after tensile fracture reveals massive {112}<111> twin. a, EBSD-IPF map showing numerous micrometer sized twins (indicated by black arrow), the tensile direction is vertical. **b,** ECCI image of the doted area in **a**. **c, d,** the enlarged IPFs and related point-to-point misorientation profile along the denoted lines corresponds to blue and red doted area in **b**, the misorientation of 60° indicates the {112}<111> twinning system.

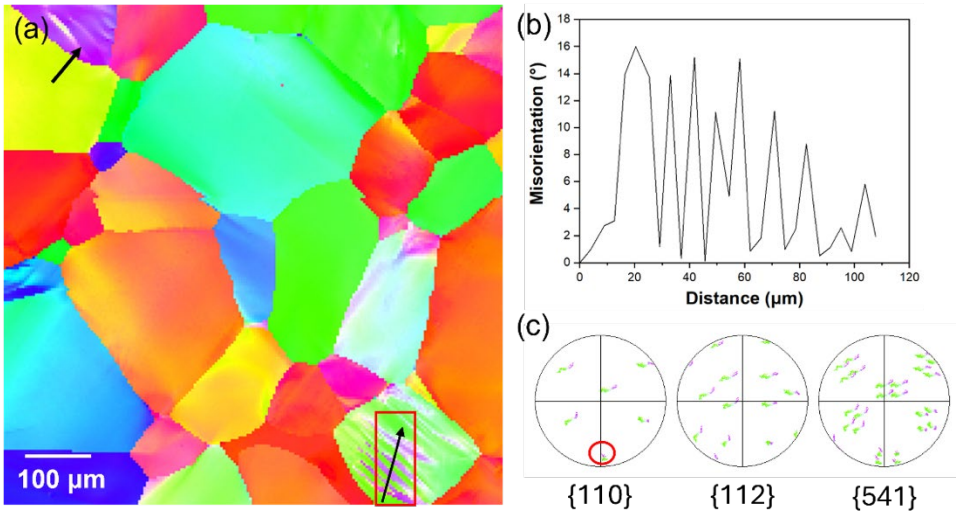

Fig. S4. Kink band intragranular misorientation axis analysis. a, IPF map from the gauge section of the homogenized tensile sample after tensile test. **b**, misorientation profile (relative to the first point) along the line inset in **a**, **c**, {011}, {112} and {541} pole figures of the rectangular subset. The {112}<111> dislocation slip system was determined.

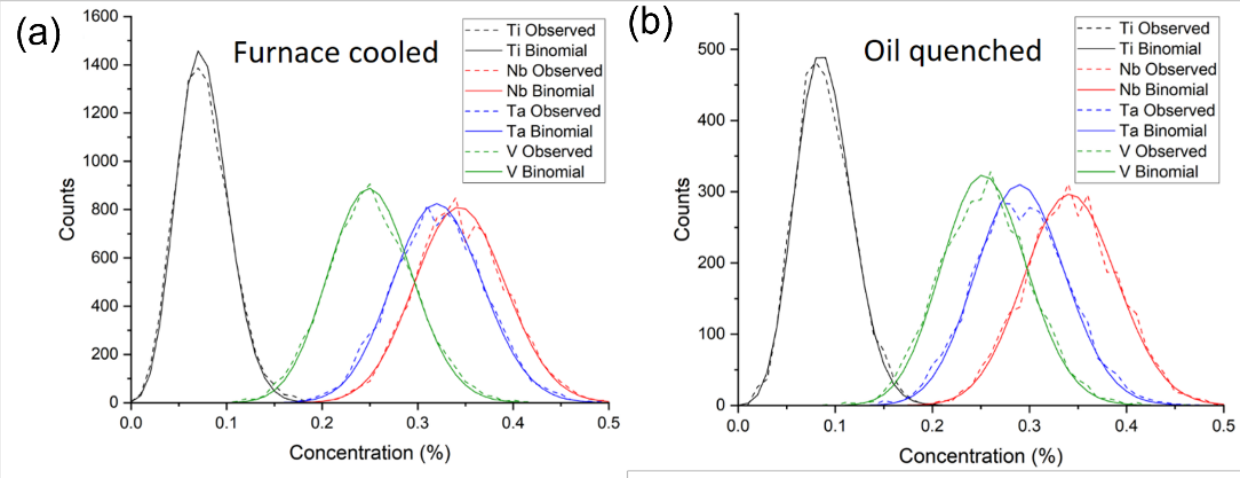

Fig. S5. Frequency distribution analysis for each element in $Nb_4Ta_4V_3Ti_1$. No significant deviation from the binomial was observed in furnace cooled **(a)** and oil quenched **(b)** specimens, indicating randomly distributed elements. The perturbations seen in the observed data (dashed lines) are not statistically significant to conclusively claim clustering tendency in these samples.

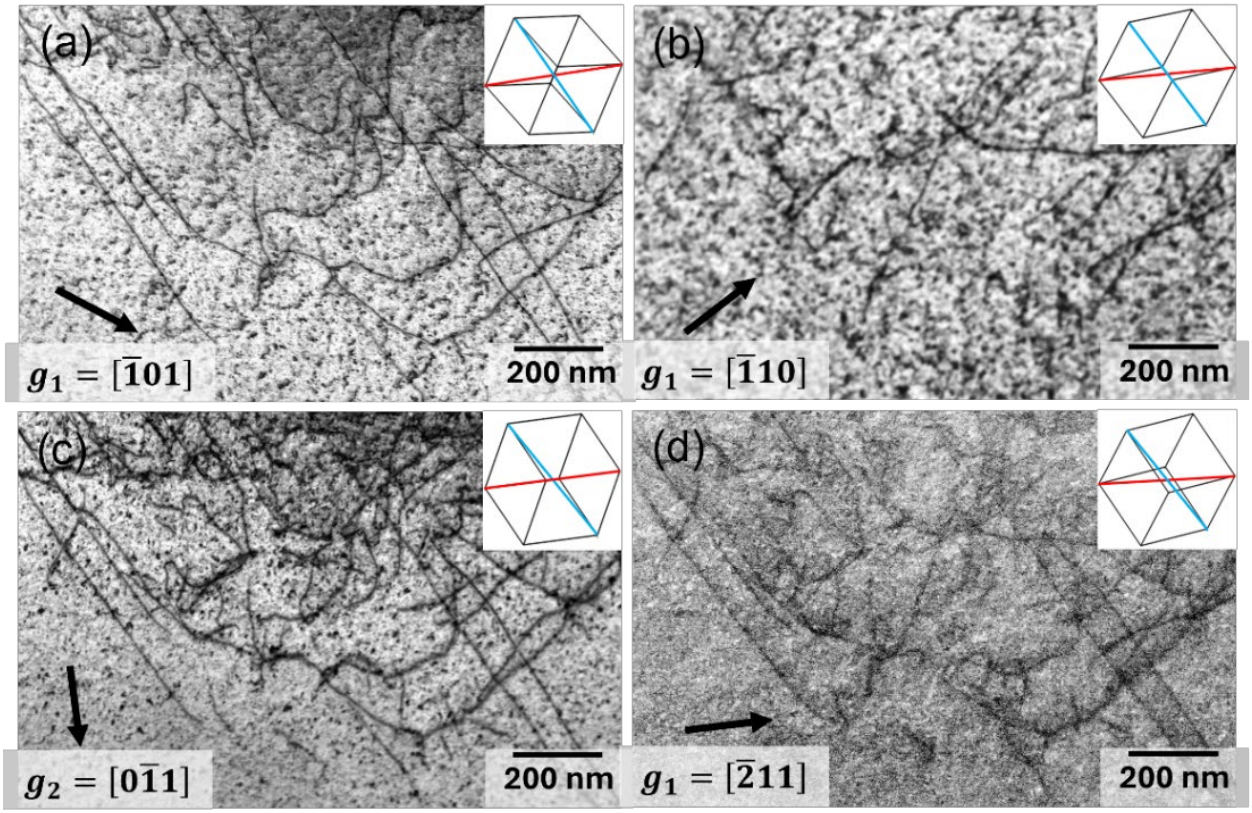

Fig. S6. Two-beam bright-field TEM images of bounded area in Fig. 3c. The diffraction vector *g* are indicated by the arow in each figure. The corresponding crystal orientation with indicated Burgers vectors are also shown in the inset.

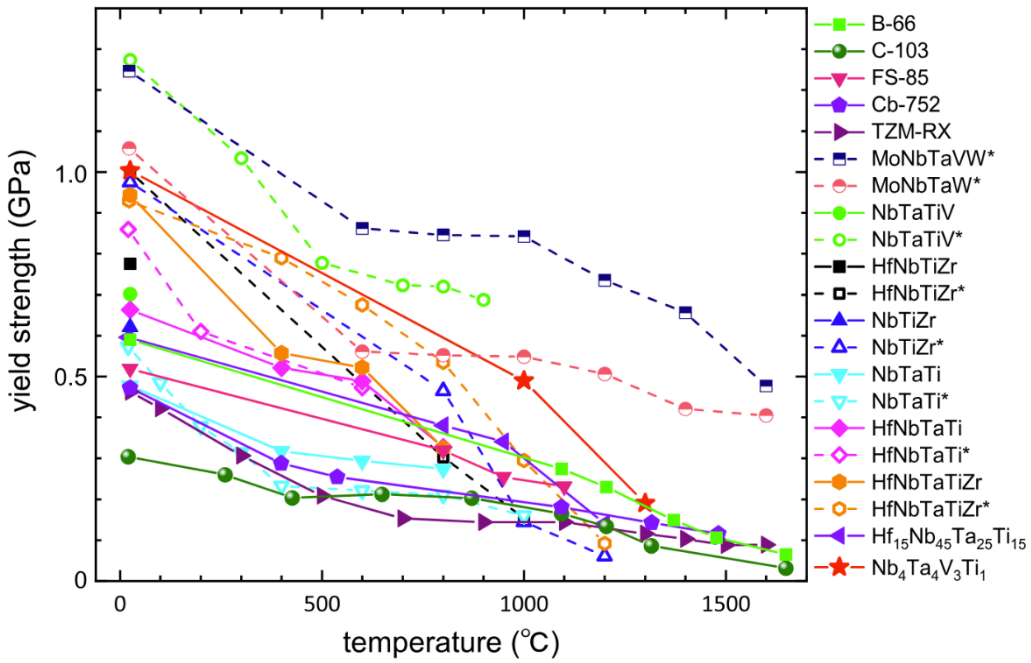

Fig. S7. Complementary figure of the dependence of yield strength on temperature for commercial refractory alloys and RMPEAs. Considering the limited data of high-temperature tensile test on RMPEAs, we added the high-temperature compressive data of some representative RMPEAs (with room-temperature tensile ductility) and the classical thermal resistant RMPEAs MoNbTaWV and MoNbTaW to enable a comprehensive assessment of the temperature dependence of mechanical behavior for the designed $Nb_4Ta_4V_3Ti_1$ alloy. The dashed lines are data from compressive tests (marked by *). The yield strength obtained from compressive tests is usually larger (100 ~ 300 MPa) than that from tensile tests (see HfNbTiZr, NbTiZr, NbTaTi, and HfNbTaTi). Since homogenization treatment only brings about subtle variation in strength in our equiatomic counterpart NbTaTiV, the abnormally large compressive yield strength (500 MPa more than tensile yield strength) should ascribe to the high impurities concentration (1.15 at.% O and 0.45 at.% N:) in the corresponding sample[3,4]. All the detailed information for the above compositions is summarized in **Table.S3**.

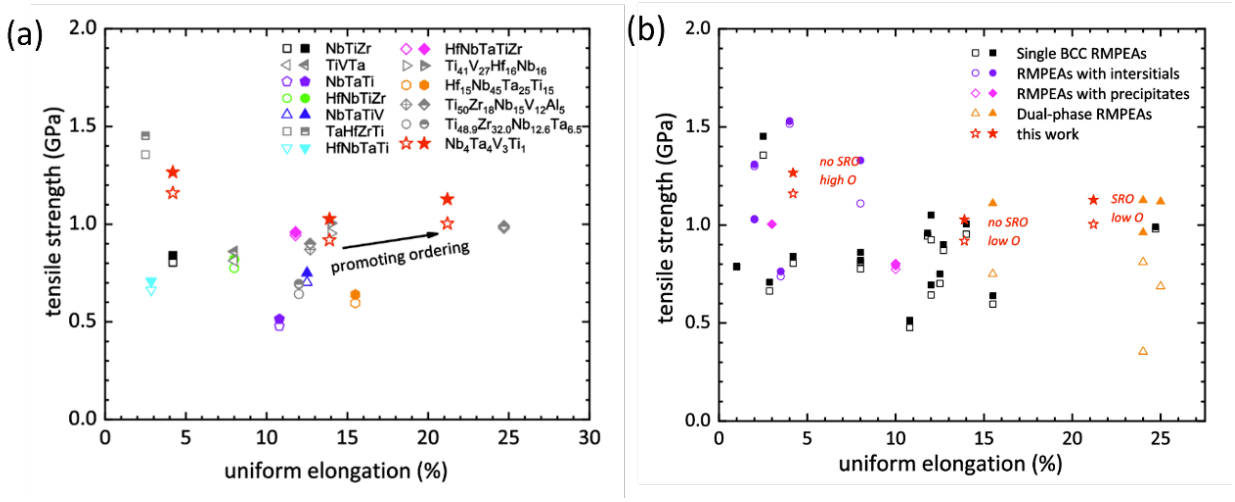

Fig. S8. Complementary Ashby charts for room-temperature strength-ductility comparisons. Two additional Ashby charts are provided to allow for thorough evaluation of the mechanical performance for the proposed $Nb_4Ta_4V_3Ti_1$ RMPEA and the effect of chemical ordering. The room-temperature tensile strength (solid for σ_y and hollow for σ_{UTS}) versus uniform elongation (ε_f) for single BCC phase RMPEAs (**a**) and RMPEAs including single phase, interstitials doped, and precipitates strengthened, and dual-phase RMPEAs (**b**). No high-temperature mechanical behavior has been reported so far on the alloys denoted by gray symbols in **a**. The uniform tensile elongation values are extracted from engineering stress-strain curves, or the intersection of true stress-strain and working hardening rate curves. We summarize in **Table. S4** all the detailed information for the above compositions.

Table. S1. Summary of the grain size, oxygen and nitrogen concentrations, and tensile behaviors of $Nb_4Ta_4V_3Ti_1$ specimens under different thermal mechanical processing. The grain sizes were determined from electron backscattered diffraction (EBSD) images. The interstitials O and N concentrations were determined by Leco system through inert gas fusion. The room-temperature yield strength σ_y, ultimate tensile strength σ_{UTS}, uniform elongation ε_u, and elongation to fracture ε_f were determined from the uniaxial engineering stress-strain curves.

Sample processing history	d (μm)	O (wppm)	N (wppm)	σ_y (MPa)	σ_{UTS} (MPa)	ε_u (%)	ε_f (%)
as-cast + 1400℃@24h homogenization with Yttrium, furnace cooling	149 ± 82	34	78	1003	1127	21.2	29.4
Homogenization + 65%CR + 1200℃@24h annealing, oil quenching	37 ± 13	420	85	1159	1265	4.2	4.2
Homogenization + 65%CR + 1200℃@24h annealing + 1400℃@24h annealing with Yttrium, oil quenching	227 ± 102	31	49	918	1027	13.9	20.7

Table. S2. The $\boldsymbol{g \cdot b}$ table for the employed diffraction vectors under zone axis ZA [111]. A zero value indicates the dislocation is invisible under the diffraction condition.

Burgers vector $\boldsymbol{b}$	$\boldsymbol{g}$ $(\bar{1}01)$	$\boldsymbol{g}$ $(0\bar{1}1)$	$\boldsymbol{g}$ $(\bar{1}10)$	$\boldsymbol{g}$ $(\bar{2}11)$
$\mathbf{1/2}\,[111]$	0	0	0	0
$\mathbf{1/2}\,[11\bar{1}]$	-1	-1	0	-1
$\mathbf{1/2}\,[1\bar{1}1]$	0	1	-1	-1
$\mathbf{1/2}\,[\bar{1}11]$	1	0	1	2

Table. S3. Strength vs temperature for commercial refractory alloys and representative BCC single phase RMPEAs. The melting point and density of RMPEAs are determined through the rule of mixture. The data of RMPEAs denoted with star (*) come from compressive tests.

Alloy and reference	Melting point (')	Density (g/cm^3)	Temperature (')	σ_y (MPa)	σ_{UTS} (MPa)
B-66[5]	2371	8.44	25	590	738
Nb-5Mo-5V-1Zr wt.%			1093	274	319
			1204	230	272
			1371	149	153
			1477	106	108
			1649	65	65
C-103[6]	2300-2400	8.86	20	304	412
Nb-10Hf-Ti-0.7Zr wt.%			260	260	370
			426.6	204	289
			648.8	212	296
			871.1	203	300
			1093.3	165	222
			1204.4	134	179

			1315.5	86.5	136
			1648.8	32	58
FS-85[7]	2590	10.61	25	519	611
Nb-28Ta-10W-1Zr wt.%			800	319	456
			950	254	381
			1100	231	333
Cb-752[5]	2425	9.03	25	472	601
Nb-10W-2.5Zr wt.%			399	288	410
			538	254	383
			1093	181	270
			1316	143	182
			1482	116	118
TZM-recrystallized[8]	2623	10.2	25	463	581
Mo-0.5Ti-0.08Zr-(0.01-0.04)C wt.%			100	422	552
			300	307	478
			500	208	410
			700	153	356
			900	144	313
			1100	144	270
			1300	116	197
			1400	103	156
			1500	88	121
			1600	89	110
NbTaTi[9]	2387	9.91	25	478	514
NbTaTi[10]			400	318	419
			600	294	378
			800	274	308
HfNbTaTi[9]	2349	10.76	25	663	709
HfNbTaTi[10]			400	521	676
			600	489	570
			800	327	372
HfNbTaTiZr[11]			25	958	974
	2250	9.91	400	557	680
HfNbTaTiZr[10]			600	522	617
			800	325	347
$Nb_{45}Ta_{25}Ti_{15}Hf_{15}$[12]	2454	10.88	20	596	640
			800	380	450
			950	341	350
			1200	140	160
HfNbTiZr*[13]	2058	8.22	25	1000	
			800	303	
			1000	154	
NbTaTiV*[3]	2268	8.96	25	1273	
			300	1034	
			500	778	
			700	723	
			800	720	
			900	688	
NbTiZr*[14]	2000	6.63	25	975	
			800	465	
			1000	145	
			1200	61	

NbTaTi*[15]	2387	9.91	20	573
			100	485
			200	378
			300	314
			400	232
			600	221
			800	210
			1000	160
HfNbTaTi*[15]	2349	10.76	20	860
			200	610
			600	473
HfNbTaTiZr*[16]	2250	9.94	23	929
			400	790
			600	675
			800	535
			1000	295
			1200	92
MoNbTaVW*[17]	2673	12.40	23	1246
			600	862
			800	846
			1000	842
			1200	735
			1400	656
			1600	477
MoNbTaW*[17]	2904	13.80	23	1058
			600	561
			800	552
			1000	548
			1200	506
			1400	421
			1600	405

Table. S4. Room-temperature tensile properties of representative RMPEAs including BCC single phase, interstitial doped, and precipitates strengthened, and dual-phase RMPEAs. The RMPEAs with reported high-temperature performance (including tensile and compressive) are denoted by *. The yield strength σ_y, ultimate tensile strength σ_{UTS}, uniform elongation ε_u, and elongation to fracture ε_f, grain size d, strain rate $\dot{\varepsilon}$, and thermal-mechanical processing history are included in the table.

Alloy and reference	σ_y **(MPa)**	σ_{UTS} **(MPa)**	ε_f **(%)**	ε_u **(%)**	**d (μm)**	$\dot{\varepsilon}$ **(s^{-1})**	**Processing history and phase**
NbTaTi*[9]	478	514	19	10.8	341	5×10^{-4}	as-cast, BCC
HfNbTaTi*[9]	663	709	11	2.86	340	5×10^{-4}	as-cast, BCC
HfNbTaTiZr*[11]	944	959	18	11.8	81	10^{-3}	as-cast + 70%CR + recrystallization, BCC
$Hf_{15}Nb_{45}Ta_{25}Ti_{15}$*[12]	596	640	35	15.5	270	10^{-3}	As-cast + 30%CR + 1100°C@1h quenching, BCC
NbTiZr*[18]	805	840	18	4.2	48	10^{-3}	as-cast, BCC
HfNbTiZr*[19]	776	821	14.3	8	N/A	2×10^{-4}	as-cast, BCC

NbTaTiV*[20]	702	750	26	12.5	206	2.5×10^{-4}	as-cast, BCC
TiVTa[20]	813	860	17	8	N/A	2.5×10^{-4}	as-cast, BCC
TaHfZrTi[21]	1356	1452	4.0	2.5	N/A	10^{-3}	as-cast, BCC
$Ti_{41}V_{27}Hf_{16}Nb_{16}$[22]	953	1005	25	4	34	10^{-3}	as-cast, BCC
$Ti_{50}Zr_{18}Nb_{15}V_{12}Al_5$ - WQ[23]	870	900	30	12.7	15	5×10^{-4}	as-cast + 1000°C@2h homogenization + 80%CR + 700°C@1h water quenching, BCC
$Ti_{50}Zr_{18}Nb_{15}V_{12}Al_5$ - Aged[23]	980	980	46.7	24.7	16.3	5×10^{-4}	as-cast + 1000°C@2h homogenization + 80%CR + 700°C@1h water quenching + 300°C@7ds furnace cooling, BCC
$Ti_{48.9}Zr_{32.0}Nb_{12.6}Ta_{6.5}$	643	694	23.8	12	120	5×10^{-4}	as-cast + 1200°C@4h homogenization + hot rolling + 70%CR + 900°C@30min, BCC
VNbTa[24]	925	1050	26	12	44	2.5×10^{-3}	as-cast, BCC
TiZrVNbAl[25]	788	788	12.8	1	230	10^{-3}	as-cast, BCC
$(NbHfZrTi)_{98}N_2$[19]	1300	1310	9.2	2	107	2×10^{-4}	as-cast, BCC
$(NbHfZrTi)_{98}O_2$[19]	1110	1330	27.7	8	70	2×10^{-4}	as-cast, BCC
$(TiZrVNbAl)_{98}O_2$[25]	1030	1030	20.9	2	245	10^{-3}	as-cast, BCC
TiZrNb-500ppm B[18]	739	764	11.6	3.5	16	10^{-3}	as-cast, BCC
$Ti_{41}V_{27}Hf_{15}Nb_{15}O_2$[22]	1517	1530	12	4	23	10^{-3}	as-cast, BCC
$Ti_{38}V_{15}Nb_{23}Hf_{24}$[26]	774	792	20.6	10	206	10^{-3}	as-cast, BCC + β*
$Ti_{38}V_{15}Nb_{23}Hf_{24}$[26]	802	802	22.5	10	176	10^{-3}	homogenization–recrystallization, BCC + β*
TiVNbHf[26]	1004	1004	16.1	3	N/A	10^{-3}	as-cast, BCC + β*
$Ta_{0.6}HfZrTi$[21]	750	1110	22.1	15.5	N/A	10^{-3}	as-cast, dual phase
$Ta_{0.5}HfZrTi$[21]	687	1119	29.9	25	N/A	10^{-3}	as-cast, dual phase
$Ta_{0.4}HfZrTi$[21]	354	1126	30.6	24	N/A	10^{-3}	as-cast, dual phase
$Ti_{52}Zr_{34}Nb_8Al_6$[27]	354	1126	30.6	24	190	5×10^{-4}	as-cast, dual phase

References

1. Stephenson, L. T., Moody, M. P., Liddicoat, P. V. & Ringer, S. P. New techniques for the analysis of fine-scaled clustering phenomena within atom probe tomography (APT) data. *Microsc. Microanal. Off. J. Microsc. Soc. Am. Microbeam Anal. Soc. Microsc. Soc. Can.* **13**, 448–463 (2007).
2. Hyde, J. M., Marquis, E. A., Wilford, K. B. & Williams, T. J. A sensitivity analysis of the maximum separation method for the characterisation of solute clusters. *Ultramicroscopy* **111**, 440–447 (2011).
3. Lee, C. *et al.* Lattice distortion in a strong and ductile refractory high-entropy alloy. *Acta Mater.* **160**, 158–172 (2018).
4. Lee, C. *et al.* Strength can be controlled by edge dislocations in refractory high-entropy alloys. *Nat. Commun.* **12**, 5474 (2021).
5. Schmidt, F. F. & Ogden, H. R. THE ENGINEERING PROPERTIES OF COLUMBIUM AND COLUMBIUM ALLOYS.
6. Jalali, S. I. A., Patullo, M. S., Philips, N. & Hemker, K. J. Capturing the ultrahigh temperature response of materials with sub-scale tensile testing. *Mater. Today* **80**, 87–100 (2024).

7. Leonard, K. J., Busby, J. T., Hoelzer, D. T. & Zinkle, S. J. Nb-Base FS-85 Alloy as a Candidate Structural Material for Space Reactor Applications: Effects of Thermal Aging. *Metall. Mater. Trans. A* **40**, 838–855 (2009).
8. Molybdenum: Properties & uses | Plansee. https://www.plansee.com/en/materials/www.plansee.com/en/materials/molybdenum.html.
9. Wang, S.-P., Ma, E. & Xu, J. New ternary equi-atomic refractory medium-entropy alloys with tensile ductility: Hafnium versus titanium into NbTa-based solution. *Intermetallics* **107**, 15–23 (2019).
10. Hsu, W.-C., Shen, T.-E., Liang, Y.-C., Yeh, J.-W. & Tsai, C.-W. In situ analysis of the Portevin-Le Chatelier effect from low to high-entropy alloy in equal HfNbTaTiZr system. *Acta Mater.* **253**, 118981 (2023).
11. Juan, C.-C. *et al.* Simultaneously increasing the strength and ductility of a refractory high-entropy alloy via grain refining. *Mater. Lett.* **184**, 200–203 (2016).
12. Cook, D. H. *et al.* Kink bands promote exceptional fracture resistance in a NbTaTiHf refractory medium-entropy alloy. *Science* **384**, 178–184 (2024).
13. Hu, Y.-M. *et al.* Microstructure and mechanical properties of NbZrTi and NbHfZrTi alloys. *Rare Met.* **38**, 840–847 (2019).
14. Senkov, O. N. *et al.* CALPHAD-aided development of quaternary multi-principal element refractory alloys based on NbTiZr. *J. Alloys Compd.* **783**, 729–742 (2019).
15. Coury, F. G., Kaufman, M. & Clarke, A. J. Solid-solution strengthening in refractory high entropy alloys. *Acta Mater.* **175**, 66–81 (2019).
16. Senkov, O. N., Scott, J. M., Senkova, S. V., Miracle, D. B. & Woodward, C. F. Microstructure and room temperature properties of a high-entropy TaNbHfZrTi alloy. *J. Alloys Compd.* **509**, 6043–6048 (2011).
17. Senkov, O. N., Wilks, G. B., Scott, J. M. & Miracle, D. B. Mechanical properties of Nb25Mo25Ta25W25 and V20Nb20Mo20Ta20W20 refractory high entropy alloys. *Intermetallics* **19**, 698–706 (2011).
18. Pang, J. *et al.* Simultaneous enhancement of strength and ductility of body-centered cubic TiZrNb multi-principal element alloys via boron-doping. *J. Mater. Sci. Technol.* **78**, 74–80 (2021).
19. Lei, Z. *et al.* Enhanced strength and ductility in a high-entropy alloy via ordered oxygen complexes. *Nature* **563**, 546–550 (2018).
20. Yin, X. *et al.* Effects of Nb Addition on Charpy Impact Properties of TiVTa Refractory High-Entropy Alloy. *Acta Metall. Sin. Engl. Lett.* **36**, 405–416 (2023).
21. Huang, H. *et al.* Phase-Transformation Ductilization of Brittle High-Entropy Alloys via Metastability Engineering. *Adv. Mater.* **29**, 1701678 (2017).
22. Cui, D. *et al.* Oxygen-assisted spinodal structure achieves 1.5 GPa yield strength in a ductile refractory high-entropy alloy. *J. Mater. Sci. Technol.* **157**, 11–20 (2023).
23. Wang, L. *et al.* Tailoring planar slip to achieve pure metal-like ductility in body-centred-cubic multi-principal element alloys. *Nat. Mater.* **22**, 950–957 (2023).
24. Han, Z. *et al.* Novel BCC VNbTa refractory multi-element alloys with superior tensile properties. *Mater. Sci. Eng. A* **825**, 141908 (2021).
25. Cui, J. *et al.* Regulate local chemical order to achieve high strength and ductility in TiZrNbVAl lightweight high entropy alloys via adding oxygen. *Mater. Sci. Eng. A* **906**, 146721 (2024).
26. Wei, S. *et al.* Natural-mixing guided design of refractory high-entropy alloys with as-cast tensile ductility. *Nat. Mater.* **19**, 1175–1181 (2020).
27. Yao, T. T., Zhang, Y. G., Yang, L., Bu, Z. Q. & Li, J. F. A metastable Ti–Zr–Nb–Al multi-principal-element alloy with high tensile strength and ductility. *Mater. Sci. Eng. A* **851**, 143646 (2022).